Inclusive spectra of stripping reactions induced by heavy ions

A. Bonaccorso
Istituto Nazionale di Fisica Nucleare, Sezione di Pisa, 56100 Pisa, Italy

I. Lhenry and T. Suomijärvi
Institut de Physique Nuclèaire, Centre National de la Recherche Scientifique–Institut National de Physique Nucleàire et de Physique des Particules F91406 Orsay, France

(Received 21 September 1993)

The spectra of inclusive transfer reactions induced by heavy ions and leading to continuum final states show high-lying broad resonancelike structures superimposed on a large continuum. Recent experimental spectra for neutron stripping on targets in the lead region are analyzed by the Bonaccorso and Brink single-particle transfer model. The results of the calculation suggest that the structures are due to the population of high-spin single-particle states which are unbound and mix with the underlying states giving rise to a broadening of the peak. The main characteristics of the spectra are reproduced. Moreover, an estimate of the elastic and inelastic breakup contributions to the inclusive spectra is given.

PACS number(s): 25.70.Hi, 24.30.Gd

I. INTRODUCTION

Transfer reactions between heavy ions at incident energies per nucleon higher than the average nucleon binding energy (~10 MeV) populate final states of the target which are unbound and give rise to a continuum spectrum. Such spectra have been measured in several experiments [1–6]. In the case of one-neutron stripping reactions, the detected kinetic energy of the ejectile is related to the kinetic energy of the emitted neutron and to the excitation energy of the target by the energy conservation relation

$$E_x = E_{\rm in} - E_f + Q_{gg} = \varepsilon_f - \varepsilon_B, \tag{1.1}$$

where E_x is the target excitation energy, $E_{\rm in}$ and E_f are the initial and final center-of-mass energies, and Q_{gg} is the ground state to the ground-state Q value. ε_f is the final neutron energy, and $\varepsilon_B < 0$ is the binding energy of the neutron in the ground state of the residual nucleus. For excitation energies $E_x < |\varepsilon_B|$, the final neutron energy is negative and we are dealing with transfer to bound states. When $E_x > |\varepsilon_B|$ the neutron final energy is positive and transfer populates continuum states. In the latter region of excitation energies, experimental spectra show several bumps superimposed on a continuum background. A large part of the background is due to direct reactions such as elastic and inelastic breakup. It is important to note that the physical background has some meaning only for $E_x > |\varepsilon_B|$, while the widths of the peaks in the region $E_x < |\varepsilon_B|$ are due only to the experimental energy resolution.

There is a model by Bonaccorso and Brink [7–10] which allows one to calculate the cross section for one-neutron transfer between initial and final single-particle states as a function of the final energy of the neutron in the continuum and that corresponds to the energy spectrum of the projectilelike fragment which is measured experimentally. One characteristic of the calculation is that at each possible final energy in the continuum the transfer probability is given by an incoherent sum of the transfer probabilities to different final angular momentum states. In this way it is possible to obtain the relative population of the single-particle states in the continuum and to make a connection between transfer to final bound states and transfer to final unbound states. In fact, transfer reactions between bound states are known to be dominated by matching conditions [11] on the energy and spin of the initial and final single-particle states and have actually been used for years to get spectroscopic information on these states. In Ref. [9] it was shown that matching conditions are also the relevant mechanism for transfer to unbound states and that measurement of transfer to the continuum can give information on the high-lying single-particle states of the nucleus. Furthermore, the Bonaccorso-Brink model allows one to distinguish the different contributions due to transfer to resonance states of the target and elastic and inelastic breakup.

The purpose of this paper is to compare the theoretical calculations made according to the Bonaccorso-Brink model to experimental spectra measured for one-neutron stripping reactions on targets in the lead region [1,4]. We wish to explain the evolution of the spectra when the incident energy increases in terms of the different reactions contributing and to give a qualitative explanation of the low-lying bumps and of the underlying background.

In Sec. II we give a brief account of the theoretical model, and in Sec. III we discuss the parametrization of the optical potential used to describe the neutron-target interaction. Section IV contains a discussion of the influence of the initial state, while Sec. V is devoted to the comparison between the spectra of several reactions performed with different projectile-target combinations at incident energies ranging from 40 to 48 MeV/nucleon. Finally, we give our conclusions in Sec. VI.

II. THEORETICAL MODEL

The model of Bonaccorso and Brink [7–10] deals with stripping reactions to a continuum final state, and it is a generalization of a model for transfer between bound states [12–14]. The initial and final states are single-particle states, and it is assumed that transfer is sensitive only to the tail of the wave functions. The relative motion of projectile and target is treated semiclassically.

The inclusive stripping spectra contain contributions from elastic breakup in which the neutron is emitted from the projectile leaving the target in the ground state, inelastic breakup in which the neutron scatters inelastically on the target, and transfer of the neutron to resonance states of the target. The relative contribution of each process to the inclusive spectrum depends on the incident energy [9,10]. At the incident energies we are concerned with in this paper, transfer to resonance states is the dominant mechanism. The spectra show large bumps, rather than narrow peaks as in transfer to bound states, because at each final energy several states with different j_f values contribute and each of them is spread over a range of final energies around its resonance energy. The calculation allows one to distinguish the contribution to the cross section due to each state of given angular momentum j_f.

The details of the formalism have been discussed in previous papers [7,8,10], while Ref. [9] was devoted to the analysis of numerical calculations. Here we give only some basic formulas.

According to Bonaccorso and Brink [9], the transfer probability from an initial bound state of definite energy ε_i, angular momentum l_i, and spin j_i to a final continuum state of positive energy ε_f is given by

$$\frac{dP}{d\varepsilon_f}(j_f,j_i) = \sum_{j_f}\langle|1-S_{j_f}|^2\rangle B(j_f,j_i) = \sum_{j_f}(|1-\langle S_{j_f}\rangle|^2 + T_{j_f})B(j_f,j_i), \quad (2.1)$$

where

$$T_{j_f} = 1 - |\langle S_{j_f}\rangle|^2.$$

$\langle S_{j_f}\rangle$ is the optical-model S matrix which describes the rescattering of the neutron on the target. The sum in Eq. (2.1) is over all possible final angular momenta corresponding to the given final energy. $B(j_f,j_i)$ is an elementary transfer probability which depends on the details of the initial and final states, on the energy of relative motion, and on the distance of closest approach between the two nuclei.

In Ref. [8] it was shown that the first term of Eq. (2.1) proportional to $|1-\langle S_{j_f}\rangle|^2$ gives the elastic breakup spectrum, while the second term proportional to the transmission coefficient T gives the absorption spectrum. The absorption is due to inelastic breakup and transfer to resonance states of the target. The method used to obtain Eq. (2.1) cannot distinguish between these two contributions, but in Ref. [10] it was shown that the inelastic breakup can be estimated by calculating the absorption in the Born approximation. This is because the inelastic breakup is a surface effect, and therefore it can be evaluated by considering only the interaction of the neutron with the tail of the optical potential and by neglecting the resonance effects which instead are due to the strong interaction of the neutron with the interior of the potential. According to Ref. [10], the inelastic breakup probability is given by

$$\frac{dP_{\rm abs}}{d\varepsilon_f} = \frac{1}{\pi\hbar^2 v^2}\mathrm{Im}\int_{-\infty}^{+\infty} d^3\mathbf{r}_2|\tilde{\psi}_1(x,y,k_1)|^2 V_2(\mathbf{r}_2), \quad (2.2)$$

where $\mathrm{Im}V_2(r)$ is the imaginary part of the optical potential used in the calculation of the S matrix in Eq. (2.1).

The calculation consists of two steps. First, one calculates Eqs. (2.1) and (2.2), and then one subtracts the spectrum obtained by Eq. (2.2) (inelastic breakup) from the second term of Eq. (2.1) proportional to the transmission coefficient T, obtaining in this way the portion of the inclusive spectrum due to transfer to resonance states of the target. This is useful to obtain an estimate of the single-particle state strength. On the other hand, by summing the elastic breakup and inelastic breakup spectra, one obtains the total nonresonant part of the spectrum, which is often referred to as the background due to direct type of reactions [2].

An approximate formula for the total transfer cross section can be obtained from Eq. (2.1) by integrating over the impact parameter of the nucleus-nucleus relative motion as in Ref. [13]:

$$\frac{d\sigma}{d\varepsilon_f} = 2\pi\int_0^\infty \frac{dP_t}{d\varepsilon_f}P_{\rm el}b\,db \approx \pi\frac{R_s-a_c}{\eta}\frac{dP_t}{d\varepsilon_f}(R_s), \quad (2.3)$$

where $dP_t/d\varepsilon_f$ is given by Eq. (2.1), R_s is the strong absorption radius, and a_c is the Coulomb length parameter. The nucleus-nucleus probability of elastic scattering [13], $P_{\rm el}$, was given by the sharp cutoff model with strong absorption radius R_s.

The calculations shown in this paper have been made for several neutron stripping reactions listed in Table I. The strong absorption radius for each reaction is also given. The final energies and angular momenta considered were $0 < \varepsilon_f < 70$ MeV and $0 < l_f < 40$, respectively.

TABLE I. Studied reactions.

Reaction	$E_{\rm inc}/u$ (MeV)	R_s (fm)
^{207}Pb(^{20}Ne,^{19}Ne)^{208}Pb	48	11.41
^{208}Pb(^{20}Ne,^{19}Ne)^{209}Pb	40	11.49
^{209}Bi(^{20}Ne,^{19}Ne)^{210}Bi	48	11.45
^{207}Pb(^{36}Ar,^{35}Ar)^{208}Pb	42	11.96
^{208}Pb(^{40}Ar,^{39}Ar)^{209}Pb	41	12.09
^{209}Bi(^{36}Ar,^{35}Ar)^{210}Bi	42	11.97

III. OPTICAL POTENTIAL

The most delicate part of the calculation is the evaluation of the optical-model S matrix which is responsible for the convergence of the sum over final angular momenta appearing in Eq. (2.1) [8,9]. In this paper we have used the following form of the real plus spin-orbit optical potential:

$$V(r) = V_R(\varepsilon_f) f(X_R) + \left(\frac{\hbar}{m_\pi c}\right)^2 V_{\text{s.o.}} \frac{1}{r}\frac{d}{dr} f(X_R) \boldsymbol{l}\cdot\boldsymbol{\sigma}, \tag{3.1}$$

while the imaginary part of the optical potential contains a volume and a surface term given by

$$W(r,\varepsilon_f) = W_V(\varepsilon_f) f(X_I) - 4a_I W_S(\varepsilon_f)\frac{d}{dr} f(X_I). \tag{3.2}$$

In both the above equations, $f(X_\alpha)$ has a Woods-Saxon shape

$$f(X_\alpha) = \left[1 + \exp\frac{r - R_\alpha}{a_\alpha}\right]^{-1},$$

with $R_\alpha = r_\alpha A^{1/3}$, $\alpha = R, I$ for the real and imaginary parts of the potential, respectively, and A is the target mass number.

The calculation of the S matrix must be very accurate at all energies; otherwise, spurious peaks appear. Furthermore, some of the optical potential parameters must be energy dependent. The values of the potential parameters which do not depend on energy are given in Table II.

A very detailed discussion of the search for the best optical potential parameters used to fit the experimental spectra can be found in Lhenry [1] and in Ref. [9]. In both these works, we followed the parametrization of the neutron-^{208}Pb optical potential given by Mahaux and Sartor [15]. Reference [15] contains also a very detailed study of the resonance states of ^{208}Pb.

The imaginary volume and surface depths that we use in this paper are both negative and energy dependent, and they were obtained using Eqs. (2.1), (2.3a), and (6.1a) of Ref. [15]. The Mahaux-Sartor parametrization is related to the Brown-Rho [16] parametrization of the imaginary volume depth, which contains a parameter whose value is close to the Fermi energy of the nucleus considered. For ^{207}Pb we have used $E_f = -7$ MeV.

The parameters used in Ref. [1] differ from those of Ref. [9] for the use of a real potential depth and a real potential radius which both depend on the energy. In order to be consistent with the discussion of Mahaux and Sartor, the real potential radius should be energy dependent if the real potential depth is energy dependent.

TABLE II. Optical-model parameters.

$V_{\text{s.o.}}$ (MeV)	r_R (fm)	a_R (fm)	r_I (fm)	a_I (fm)
9	1.25	0.55	1.275	0.3

However, if the radius decreases with energy as proposed by Mahaux and Sartor, less partial waves contribute to the sum in Eq. (2.1), and as a consequence we do not reproduce well the tail of the experimental spectra as was shown in Ref. [1]. This apparent inconsistency is due to the fact that we have already reduced the number of high j_f values contributing to (2.1) by using a real and imaginary diffuseness which are smaller than those used by Mahaux and Sartor. This was done to secure the convergence of the sum in Eq. (2.1) as discussed in detail in Ref. [8]. Therefore in this paper we keep the real potential radius constant and we use instead a parametrization for the real potential depth, which is different from the parametrization of Ref. [1]. It is important to note [9] that the real part of the potential has to be chosen such that it gives the correct sequence and the correct energies of the single-particle states in the target. According to Mahaux and Sartor, the real potential is given by the sum of a volume term and a surface term called the polarization potential. Because of the Fermi-surface anomaly, the depth of the polarization potential has a maximum around the Fermi energy [15] and we have found that an effective way of taking it into account is to use the following parametrization for the energy dependence of the Woods-Saxon potential of Eq. (3.1):

$$\begin{aligned} V_R &= -45.8 - (0.3\varepsilon_f - 3), \quad \varepsilon_f = 1\text{–}10 \text{ MeV}, \\ V_R &= -45.8, \quad \varepsilon_f = 10\text{–}20 \text{ MeV}, \\ V_R &= -45.8 + (0.1\varepsilon_f - 1), \quad \varepsilon_f > 20 \text{ MeV}. \end{aligned} \tag{3.3}$$

In Ref. [1] the results obtained using an energy-dependent real potential depth were compared to those obtained using a constant real potential depth and it was shown that using an energy-dependent V_R gives an improvement in the position of the first bump, while it does not change much the behavior of the rest of the spectra. This is because the high-energy part of the spectra is given mainly by the terms corresponding to high j_f values in the sum in Eq. (2.1) and they depend upon the tail of the optical potential but not on its depth.

In Table III we give the sequence of bound and resonance states obtained in the real plus spin-orbit part of

TABLE III. Neutron levels in ^{208}Pb obtained in the real part of the potential of Table II.

State	ε (MeV)
$1k_{17/2}$	5.8
$1j_{13/2}$	5.3
$2h_{11/2}$	2.7
$3d_{3/2}$	−0.44
$2g_{7/2}$	−0.65
$4s_{1/2}$	−1.18
$3d_{5/2}$	−1.97
$1j_{15/2}$	−3.60
$1i_{11/2}$	−3.94
$2g_{9/2}$	−4.44

TABLE IV. Initial-state parameters.

Initial state	ε_i (MeV)	γ_i (fm^{-1})	C^2S	C_i (fm$^{-1/2}$)	l_i
$(^{19}\mathrm{Ne}+n)_{2s_{1/2}}$	−16.86	0.901	0.56	20.99	0
$(^{19}\mathrm{Ne}+n)_{1d_{5/2}}$	−17.10	0.907	1.03	7.75	2
$(^{19}\mathrm{Ne}+n)_{1p_{1/2}}$	−17.14	0.908	1.96	10.42	1
$(^{35}\mathrm{Ar}+n)_{1d_{3/2}}$	−15.25	0.857	2.92	11.12	2
$(^{35}\mathrm{Ar}+n)_{2s_{1/2}}$	−16.43	0.877	2.5	30.87	0
$(^{35}\mathrm{Ar}+n)_{2p_{3/2}}$	−17.88	0.915	0.12	36.94	1
$(^{39}\mathrm{Ar}+n)_{1f_{7/2}}$	−9.87	0.681	0.54	2.69	3
$(^{39}\mathrm{Ar}+n)_{2p_{3/2}}$	−11.14	0.732	0.1	16.67	1
$(^{39}\mathrm{Ar}+n)_{1d_{3/2}}$	−11.39	0.741	2.2	7.17	2
$(^{39}\mathrm{Ar}+n)_{2s_{1/2}}$	−12.25	0.768	1.26	21.07	0

the potential when the real depth is taken, $V_R = -45.8$ MeV. The sequence of the states shown in Table III agrees with the single-particle levels obtained for ^{208}Pb by using the quasiparticle-phonon model [2]. However, we note that our bound states have energies lower by about 1 MeV than the energies of Ref. [2]. This effect cannot be corrected within the above parametrization, and it affects the calculated spectra, as will be discussed in Sec. V.

IV. INFLUENCE OF THE INITIAL STATE

Another important point of the calculation is the choice of the initial state. In Ref. [9] it was shown that the shape of the transfer spectra depends on the initial bound state of the neutron in the projectile. In particular, it was shown that for obtaining a good agreement between the calculation and experiment it is important to sum the contributions of transfer from several possible occupied states of the projectile which leave the ejectile with excitation energies smaller than the energy threshold for particle emission. The initial-state parameters used in the calculations of this paper are given in Table IV. The spectroscopic factors were taken from Refs. [17,18]. There are uncertainties in the values of the spectroscopic factors, and this affects the shape of the spectra calculated in this paper. In the case of the ^{40}Ar-induced reaction, we have found disagreement between the experimental spectrum and the calculated spectrum if we include the $2s_{1/2}$ initial state. This problem is discussed in more detail in the next section.

Figures 1 and 2 are relative to the reaction ^{207}Pb(^{20}Ne,^{19}Ne)^{208}Pb, and they illustrate the initial-state dependence. Figure 1 shows the so-called projectile form factor for three possible initial particle states in ^{20}Ne, namely, the $2s_{1/2}$, $1p_{1/2}$, and $1d_{5/2}$. The projectile form factor appears in the definition of the elementary transfer probability $B(j_i, j_f)$ of Eq. (2.1), and it is proportional to the Fourier transform of the initial-state wave function [9]. Its explicit expression is

$$F(k_1) = |C_i|^2 e^{-2\eta R_i} P_{l_i}(X_i), \tag{4.1}$$

where

$$k_1 = -\frac{(\varepsilon_i - \varepsilon_f + \frac{1}{2}mv^2)}{\hbar v}. \tag{4.2}$$

k_1 is the neutron momentum relative to the initial nu-

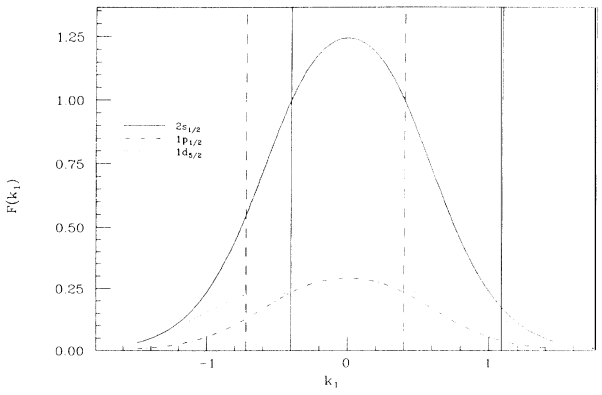

FIG. 1. ^{20}Ne form factors calculated according to Eq. (4.1). The solid curve is for the $2s_{1/2}$ single-particle state, the dot-dashed curve is for the $1p_{1/2}$ state, and the dotted curve is for the $1d_{5/2}$ state. Solid and dashed vertical lines mark out the range of k_1 values relevant to a reaction at E_{inc}=48 and 80 MeV/nucleon, respectively.

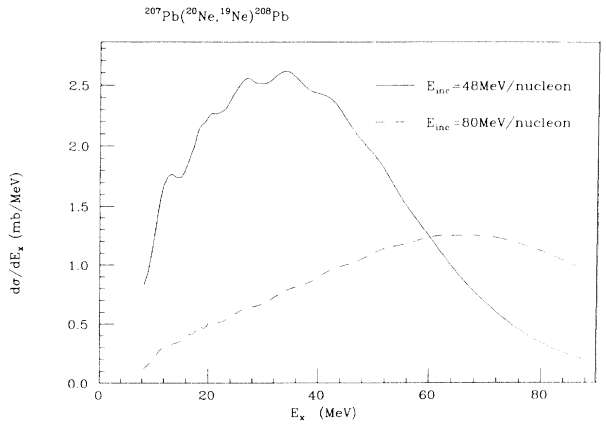

FIG. 2. Calculated spectra of the reaction ^{207}Pb(^{20}Ne,^{19}Ne)^{208}Pb at E_{inc}=48 MeV/nucleon (solid curve) and at E_{inc} = 80 MeV/nucleon (dashed curve).

cleus, and ε_i and ε_f are the energies of the neutron in the initial bound state and in the final continuum state, respectively, while $\frac{1}{2}mv^2$ is the incident energy per nucleon at the distance of closest approach. R_i is the projectile radius, and C_i is the asymptotic normalization constant of the initial-state wave function.

Given a range of final continuum energies, the range of k_1 values which are relevant to the calculation is different depending on the incident energy of the reaction. As an example, in Fig. 1 we mark out the k_1 range relative to $E_{\rm inc}$=48 MeV/nucleon with the solid lines, while the dashed lines indicate the range relative to $E_{\rm inc}$ = 80 MeV/nucleon. In both cases the range of final continuum energies is $0 < \varepsilon_f < 80$ MeV. The maximum transfer probability and then the maximum of a calculated spectrum correspond to a maximum in the intial-state form factor, and from Fig. 1 one can note that both the $2s_{1/2}$ and $1p_{1/2}$ distributions have maxima for $k_1 = 0$. From Eqs. (1.1) and (4.2), using the values of ε_i given in Table IV and $\varepsilon_B = -7.3$ MeV, which is the neutron separation energy in ^{208}Pb, we get that $k_1 = 0$ corresponds to $\varepsilon_f \sim 26$ MeV and $E_x \sim 33$ MeV when $E_{\rm inc}$=48 MeV, while it corresponds to $\varepsilon_f \sim 58$ MeV and $E_x \sim 65$ MeV when $E_{\rm inc} = 80$ MeV. This effect is reflected in the shape of the energy spectra as shown in Fig. 2. The solid line gives the spectrum at $E_{\rm inc}$=48 MeV/nucleon, and it has a maximum at $E_x \sim 33$ MeV as expected, while the dashed line is the spectrum at $E_{\rm inc}$=80 MeV/nucleon, and it has a maximum at $E_x \sim 65$ MeV. Figures 1 and 2 show that given a certain combination of projectile and target, by changing the projectile incident energy, transfer reactions can probe different regions of the momentum distribution of the neutron in the projectile nucleus.

The fact that the ejectile energy spectra reflect the momentum distributions of the neutron on the surface of the projectile was already noticed in Ref. [9]. It is a characteristic of the reactions having a continuum final state which appears clearly at very high incident energies when the breakup becomes the dominant contribution [19,20]. The situation is more complicated at the incident energies considered in this paper because the absorption into resonance states, which affects the low-energy part of the spectra, is still large.

V. COMPARISONS WITH EXPERIMENTAL SPECTRA

In this section we compare the calculated spectra to the experimental spectra for the reactions listed in Table I. These reactions were studied at the GANIL national facility, Caen, France. The use of the energy-loss magnetic spectrometer SPEG allowed us to measure the transfer spectra with a good energy resolution (500 keV for Ne and 700 keV for Ar beams). All spectra were measured in an angular range of 4° around the grazing angle. Absolute cross-section values were available only in the case of ^{207}Pb(^{20}Ne,^{19}Ne)^{208}Pb and ^{207}Pb(^{36}Ar,^{35}Ar)^{208}Pb reactions. However, in heavy-projectile-induced reactions, most of the cross section is focused to forward angles and the shape of the energy spectra is independent of the scattering angle. Therefore the shape of the experimental spectra can be directly compared to the spectra calculated according to Eq. (2.3), which gives the angle-integrated cross section.

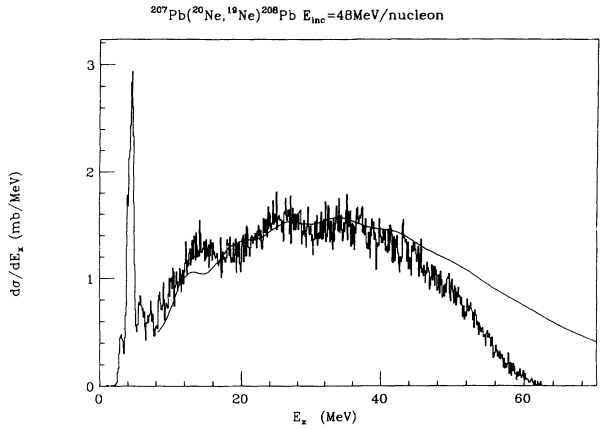

FIG. 3. Angle-integrated experimental and calculated energy cross sections of the reaction ^{207}Pb(^{20}Ne,^{19}Ne)^{208}Pb at $E_{\rm inc}$ = 48 MeV/nucleon. The solid line gives the calculated spectrum which has been multiplied by a factor 0.6 to fit the experimental spectrum.

Figures 3 and 4 show the integrated spectra of the reactions ^{207}Pb(^{20}Ne,^{19}Ne)^{208}Pb at $E_{\rm inc}$ = 48 MeV/nucleon and ^{207}Pb(^{36}Ar,^{35}Ar)^{208}Pb at $E_{\rm inc}$ = 42 MeV/nucleon, respectively. In the first case, the calculated spectrum has been normalized by a factor 0.6 in order to fit the experimental spectrum, while in the second case the normalization factor is 0.16. These values are rather good compared to the uncertainty on the absolute experimental normalization, which is around 30%, and considering that the calculated spectrum is very sensitive to the value of the strong absorption radius R_s as discussed in Ref. [9].

Figure 5 shows experimental spectra measured for different reactions together with the calculated spectra,

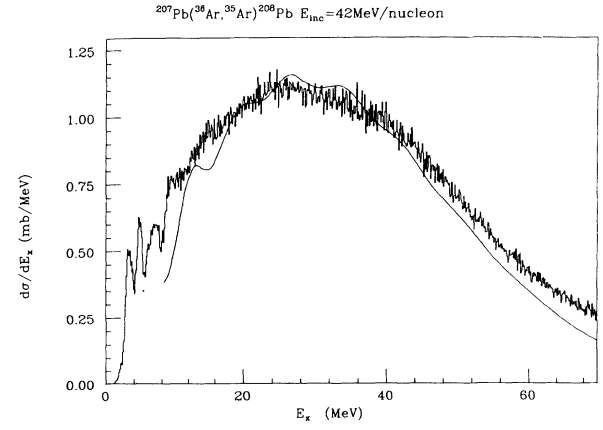

FIG. 4. Angle-integrated experimental and calculated energy cross sections of the reaction ^{207}Pb(^{36}Ar,^{35}Ar)^{208}Pb at $E_{\rm inc}$=42 MeV/nucleon. The solid line gives the calculated spectrum, which has been multiplied by a factor 0.16 to fit the experimental spectrum.

which were arbitrarily normalized to the experimental results. The overall shape of the experimental spectra is reproduced reasonably well by the calculations. It should be noted that the discrepancies between the calculation and experiment in the cases of the reactions ^{207}Pb(^{20}Ne,^{19}Ne)^{208}Pb and ^{208}Pb(^{20}Ne,^{19}Ne)^{209}Pb were due to an experimental cutoff for energies larger than 50 MeV. The spectra for the Ne-induced reactions show a pronounced bump centered between 11 and 14 MeV depending on the target. The bump in the calculation is centered at an excitation energy which is lower by about 2 MeV than that in the experimental spectra. This is related to the energy shift for the bound states that we discussed at the end of Sec. III. The first bump observed in the calculation is due mainly to the excitation of the $1k_{17/2}$, $1l_{19/2}$, and $1m_{21/2}$ resonances in Pb which contribute to the cross section for 48%, 20%, and 7%, respectively. Also, the $j_{13/2}$ and $j_{15/2}$ states together give

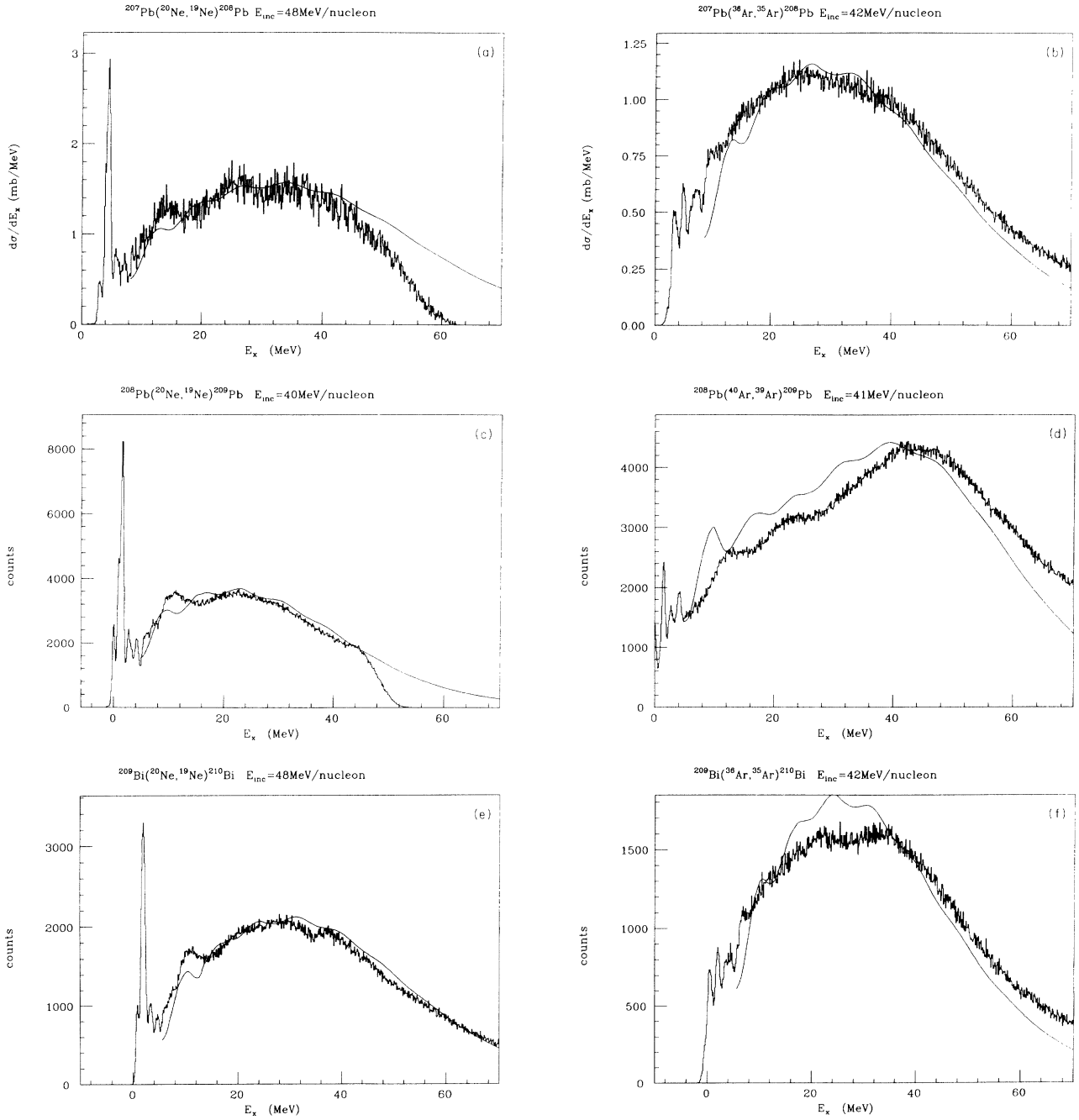

FIG. 5. Comparison between the experimental and calculated spectra studied in this paper; all calculations have been arbitrarily normalized to the data: (a) ^{207}Pb(^{20}Ne,^{19}Ne) ^{208}Pb at E_{inc}=48 MeV/nucleon, (b) ^{207}Pb(^{36}Ar,^{35}Ar)^{208}Pb at E_{inc}=42 MeV/nucleon, (c) ^{208}Pb(^{20}Ne,^{19}Ne)^{209}Pb at E_{inc}=40 MeV/nucleon, (d) ^{208}Pb(^{40}Ar,^{39}Ar)^{209}Pb at E_{inc}=41 MeV/nucleon, (e) ^{209}Bi(^{20}Ne,^{19}Ne)^{210}Bi at E_{inc}=48 MeV/nucleon, and (f) ^{209}Bi(^{36}Ar,^{35}Ar)^{210}Bi at E_{inc}=42 MeV/nucleon.

a contribution of 7%. This result is in agreement with the microscopic calculations of Ref. [21], where it was shown that most of the cross section at this excitation energy is due to the population of the $1k_{17/2}$ state.

At higher excitation energies, the calculations give several broad low-amplitude structures, which, however, remain inside the statistical fluctuation of the experimental spectra. In the calculation one gets a bump whenever the final energy of the neutron in the continuum is close to the energy of a single-particle resonance of angular momentum j_f. Then that final j_f state is populated with a probability which is much larger than the probability for other underlying single-particle states.

Now we would like to come back to the problem with the ^{40}Ar-induced reaction that we mentioned in the previous section. Figure 6 shows the spectra that one obtains considering the four possible initial states of ^{40}Ar given in Table IV. The solid curve is relative to the s initial state, the dotted curve is for the d initial state, the dashed curve is for the p initial state, and finally the close dotted curve is for the f initial state. Each curve has been multiplied by the appropriate spectroscopic factor according to Table IV. The s-initial-state spectrum gives a large cross section because of the large asymptotic normalization constant. Furthermore, it is centered at a lower energy than the d-initial-state spectrum. If we take the s state into account, the total spectrum is given by the dashed curve in Fig. 7, while the solid curve is the total spectrum without the contribution from the s initial state. The use of other spectroscopic factors has not improved the agreement between calculation and experiment. This anomaly suggests that the largest part of the $2s_{1/2}$ strength could be centered at an energy higher than the particle-emission threshold in ^{39}Ar, and then it would not contribute to the experimental spectrum. The dot-dashed curve in Fig. 7 is the spectrum obtained taking into account only the d initial state. This is the calculated spectrum which agrees best with the experimental spectrum, and it shows that in ^{40}Ar-induced transfer reactions the contribution from the d initial state is dominant.

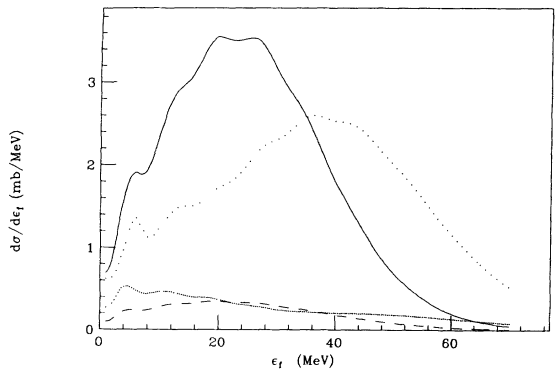

FIG. 6. Calculated spectra of the reaction ^{208}Pb(^{40}Ar,^{39}Ar)^{209}Pb at $E_{\rm inc}$=41 MeV/nucleon. The solid curve is the spectrum obtained considering only the $2s_{1/2}$ initial state, the dotted curve is relative to the $1d_{3/2}$ initial state, the dashed curve is for the $2p_{3/2}$ initial state, and the close dotted curve is for the $1f_{7/2}$ initial state. Each calculated spectrum has been multiplied by the appropriate spectroscopic factor given in Table IV.

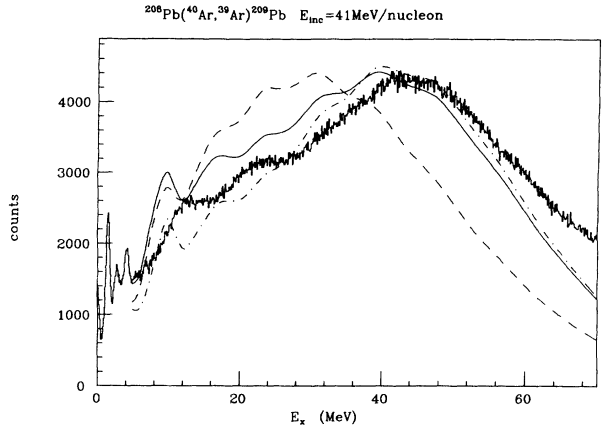

FIG. 7. Experimental spectrum of the reaction ^{208}Pb(^{40}Ar,^{39}Ar)^{209}Pb at $E_{\rm inc}$=41 MeV/nucleon compared to calculated spectra. The dashed line is the result of the calculation in which the spectra for all initial states shown in Fig. 6 have been summed. The solid line is the calculation in which the s state has been neglected, while the dot-dashed curve is the calculation including only the d state. All calculated spectra have been arbitrarily normalized to the data.

Finally, Figs. 8 and 9 illustrate the possibility to distinguish in the inclusive spectra the components due to different reactions. Figure 8 is for the reaction ^{207}Pb(^{36}Ar,^{35}Ar)^{208}Pb at $E_{\rm inc}$=42 MeV/nucleon, while Fig. 9 is for the reaction ^{209}Bi(^{20}Ne,^{19}Ne)^{210}Bi at $E_{\rm inc}$=48 MeV/nucleon. In both figures curve a gives the elastic breakup spectrum of the neutron from the

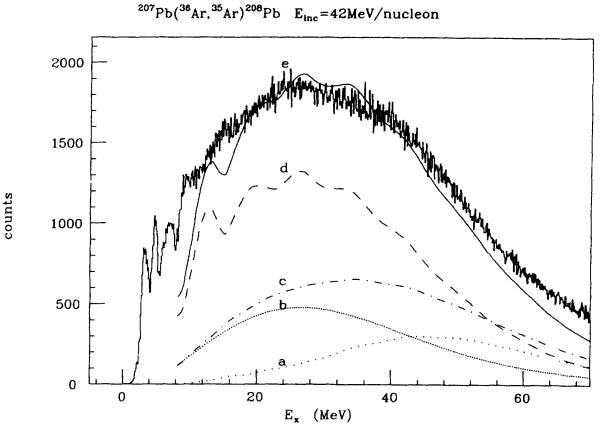

FIG. 8. Experimental spectrum of the reaction ^{207}Pb(^{36}Ar,^{35}Ar)^{208}Pb at $E_{\rm inc}$=42 MeV/nucleon compared to the calculated inclusive spectrum given by curve e. Curve a gives the elastic breakup spectrum calculated from the first term of Eq. (2.1); curve b gives the inelastic breakup spectrum calculated from Eq. (2.2). Curve c is the sum of the elastic and inelastic spectra, while curve d gives the spectrum for transfer to resonance states of the target obtained by subtracting from the inclusive spectrum (curve e) the total breakup spectrum (curve c).

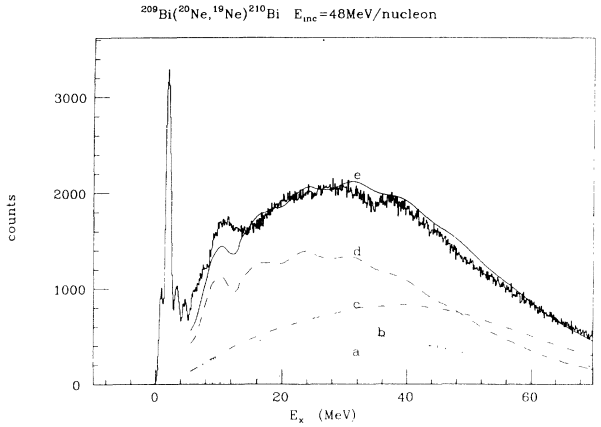

FIG. 9. Comparison between experimental and calculated spectra of the reaction ^{209}Bi(^{20}Ne,^{19}Ne)^{210}Bi at $E_{\rm inc}$=48 MeV/nucleon. The notation is the same as for Fig. 8.

projectile calculated according to the first term of Eq. (2.1). Curve *b* gives the inelastic breakup in which the target is excited by the final-state interaction of the neutron from the projectile. It is calculated according to Eq. (2.2). The sum of elastic and inelastic breakup is given by curve *c*, and it is an estimate of the background due to direct reactions. Subtracting this contribution from the total inclusive cross section given by curve *e* and calculated according to Eq. (2.1), we obtain the transfer spectrum corresponding to the absorption of the neutron into the single-particle resonance states of the target. This is curve *d* in Figs. 8 and 9. It is interesting to note that the oscillations in this part of the spectra disappear for energies larger than 40 MeV. This is due to the saturation of the imaginary part of the neutron-target optical potential [15], which gives a complete damping of the single-particle states. Figure 9 is interesting because it shows that when the incident energy increases, in this case $E_{\rm inc}$=48 MeV/nucleon, the maximum of the total breakup spectrum (curve *c*) moves toward higher excitation energy compared to the case shown in Fig. 8 where $E_{\rm inc}$=42 MeV/nucleon. In both cases the maximum of the breakup spectrum is centered at an excitation energy whose value corresponds to the incident energy per nucleon and it has a magnitude of about one-third of the inclusive cross section. In the low-energy part of the spectra, instead, the background is about one-tenth of the inclusive cross section. This is because transfer reactions to single-particle resonance states dominate. This result is in agreement with the results of a recent experiment in which the decay of the first bump at $E_x \sim 10$ MeV in the reaction ^{208}Pb(α,^{3}He)^{209}Pb at $E_{\rm inc}$=122 MeV was studied by measuring in coincidence the ejectile and neutrons emitted at backward angles [22].

VI. CONCLUSIONS

Several one-neutron stripping reactions to the continuum have been analyzed for targets in the lead region. The incident energies varied in the range 40–48 MeV/nucleon and the projectiles were ^{20}Ne, ^{36}Ar, and ^{40}Ar. The theoretical calculations were done according to the Bonaccorso-Brink model, which gives a single-particle picture of the transfer reaction. It allows one to calculate the one-neutron transfer cross section as a function of the final energy of the neutron in the continuum corresponding to the energy spectrum of the projectile-like fragment measured experimentally.

We have shown that all spectra can be reproduced quite well provided one uses a good parametrization for the energy dependence of the optical potential describing the neutron rescattering on the target. The resonance-like structures in the spectra are due to high-spin single-particle states which have a large probability of being populated by transfer. The structures are wide because several final states of different j_f values are populated at the same final energy and none of them exhausts more than 50% of the transfer cross section. The number of structures and their positions in each spectra depend just on the matching conditions that relate the initial- and final-state energies and spins. In this respect transfer to the continuum is very similar to transfer to a final bound state.

The inclusive spectra in the continuum region contain a physical background due to direct reactions. The Bonaccorso-Brink model takes into account the final-state interaction of the transferred neutron with the target, and therefore it treats consistently direct reactions and transfer to resonance states. We have shown that direct reactions account for a small part of the cross section at low excitation energy, but they become stronger around the excitation energy corresponding to the incident energy per nucleon. This is the optimum Q-value effect discussed in [7–9]. On the other hand, transfer to single-particle resonance states of the target is the most important reaction mechanism at low excitation energies.

[1] I. Lhenry, Ph.D. thesis, Report No. IPNO-T92-01, Orsay, 1992; I. Lhenry, T. Suomijärvi, Y. Blumenfeld, Ph. Chomaz, N. Frascaria, J. P. Garron, J. C. Roynette, J. A. Scarpaci, D. Beaumel, S. Fortier, S. Gàles, H. Laurent, A. Gillibert, G. Crawley, J. Finck, G. Yoo, and J. Barreto (unpublished).

[2] S. Galès, Ch. Stoyanov, and A. I. Vdovin, Phys. Rep. **166**, 125 (1988), and references therein.

[3] S. Fortier, S. Gàles, S. M. Austin, W. Benenson, G. M. Crawley, C. Djalali, J. S. Winfield, and G. Yoo, Phys. Rev. C **41**, 2689 (1990).

[4] D. Beaumel, Y. Blumenfeld, Ph. Chomaz, N. Frascaria, J. P. Garron, J. C. Roynette, T. Suomijärvi, J. Barrette, B. Berthier, B. Fernandez, J. Gastebois, and W. Mittig, Annual Report No. IPN-Orsay, 1987, p. 41.

[5] W. Lahmer, W. von Oertzen, A. Miczaika, H. G. Bohlen, W. Weller, R. Glashow, R. Grzonka, R. Santo, Y. Blumenfeld, N. Frascaria, J. P. Garron, J. C. Jacmart, and J. C. Roynette, Z. Phys. A **337**, 425 (1990).

[6] G. H. Yoo, G. M. Crawley, N. A. Orr, J. S. Winfeld,

J. E. Finck, S. Galès, Ph. Chomaz, I. Lhenry, and T. Suomijärvi, Phys. Rev. C **47**, 1200 (1993).
[7] A. Bonaccorso and D. M. Brink, Phys. Rev. C **38**, 1776 (1988).
[8] A. Bonaccorso and D. M. Brink, Phys. Rev. C **43**, 299 (1991).
[9] A. Bonaccorso and D. M. Brink, Phys. Rev. C **44**, 1559 (1991).
[10] A. Bonaccorso and D. M. Brink, Phys. Rev. C **46**, 700 (1992).
[11] D. M. Brink, Phys. Lett. **40B**, 37 (1972).
[12] L. Lo Monaco and D. M. Brink, J. Phys. G **11**, 935 (1985).
[13] A. Bonaccorso, D. M. Brink, and L. Lo Monaco, J. Phys. G **13**, 1407 (1987).
[14] H. Hashim and D. M. Brink, Nucl. Phys. **A476**, 107 (1988).
[15] C. Mahaux and R. Sartor, Nucl. Phys. **A493**, 157 (1989).
[16] G. E. Brown and M. Rho, Nucl. Phys. **A372**, 397 (1981).
[17] T. Engeland and P. J. Ellis, Nucl. Phys. **A181**, 368 (1972).
[18] R. R. Johnson and R. J. Griffiths, Nucl. Phys. **A108**, 113 (1968).
[19] J. Hüfner and M. C. Nemes, Phys. Rev. C **23**, 2538 (1981).
[20] H. Sagawa and K. Yazaki, Phys. Lett B **244**, 149 (1990).
[21] I. Lhenry, T. Suomijärvi, Ph. Chomaz, and Nguyen van Giai, Nucl. Phys. A (to be published).
[22] D. Beaumel, S. Fortier, S. Galès, J. Guillot, H. Langevin-Joliot, H. Laurent, J. M. Maison, J. Vernotte, J. Bordewijck, S. Brandenburg, A. Krasznahorkay, G. M. Crawley, C. P. Massolo, and M. Renteria (private communication).